

Symmetry-dependent ultrafast manipulation of nanoscale magnetic domains

Nanna Zhou Hagström¹, Rahul Jangid², Meera Madhavi², Diego Turenne³, Jeffrey A. Brock⁴, Erik S. Lamb⁵, Boyan Stoychev⁵, Justine Schlappa⁶, Natalia Gerasimova⁶, Benjamin Van Kuiken⁶, Rafael Gort⁶, Laurent Mercadier⁶, Loïc Le Guyader⁶, Andrey Samartsev⁶, Andreas Scherz⁶, Giuseppe Mercurio⁶, Hermann A. Dürr³, Alexander H. Reid⁷, Monika Arora⁸, Hans T. Nembach^{9,10}, Justin M. Shaw⁸, Emmanuelle Jal¹¹, Eric E. Fullerton⁴, Mark W. Keller⁸, Roopali Kukreja², Stefano Bonetti^{1,12}, Thomas J. Silva⁸, and Ezio Iacocca^{13,14,*}

¹*Department of Physics, Stockholm University, 106 91 Stockholm, Sweden*

²*Department of Materials Science and Engineering, University of California Davis, Davis, California 95616, USA*

³*Department of Physics and Astronomy, Uppsala University, 75120 Uppsala, Sweden*

⁴*Center for Memory and Recording Research, University of California San Diego, La Jolla, California 92037, USA*

⁵*Department of Physics, University of California San Diego, La Jolla, California 92037, USA*

⁶*European XFEL, Holzkoppel 4, 22869 Schenefeld, Germany*

⁷*Linac Coherent Light Source, SLAC National Accelerator Laboratory, Menlo Park, California 94025, USA*

⁸*Quantum Electromagnetics Division, National Institute of Standards and Technology, Boulder, Colorado 80305, USA*

⁹*Department of Physics, University of Colorado, Boulder, Colorado 80309, USA*

¹⁰*Associate of the National Institute of Standards and Technology, Boulder, Colorado 80305, USA*

¹¹*Sorbonne Université, CNRS, Laboratoire de Chimie Physique–Matière et Rayonnement, LCPMR, Paris 75005, France*

¹²*Department of Molecular Sciences and Nanosystems, Ca' Foscari University of Venice, 30172 Venezia, Italy*

¹³*Department of Mathematics, Physics, and Electrical Engineering, Northumbria University, Newcastle upon Tyne NE1 8ST, United Kingdom*

¹⁴*Center for Magnetism and Magnetic Nanostructures, University of Colorado Colorado Springs, Colorado Springs, Colorado 80918, USA*



(Received 8 July 2022; revised 25 November 2022; accepted 29 November 2022; published 23 December 2022)

Femtosecond optical pumping of magnetic materials has been used to achieve ultrafast switching and recently to nucleate symmetry-broken magnetic states. However, when the magnetic order parameter already presents a broken-symmetry state, such as a domain pattern, the dynamics are poorly understood and consensus remains elusive. Here, we resolve the controversies in the literature by studying the ultrafast response of magnetic domain patterns with varying degrees of translation symmetry with ultrafast x-ray resonant scattering. A data analysis technique is introduced to disentangle the isotropic and anisotropic components of the x-ray scattering. We find that the scattered intensity exhibits a radial shift restricted to the isotropic component, indicating that the far-from-equilibrium magnetization dynamics are intrinsically related to the spatial features of the domain pattern. Our results suggest alternative pathways for the spatiotemporal manipulation of magnetism via far-from-equilibrium dynamics and by carefully tuning the ground-state magnetic textures.

DOI: [10.1103/PhysRevB.106.224424](https://doi.org/10.1103/PhysRevB.106.224424)

I. INTRODUCTION

Ultrafast manipulation of symmetry is achievable in a wide variety of physical systems that rely on nonequilibrium pathways to access hidden states in their energy landscape. Far-from-equilibrium transitions from symmetric to symmetry-broken states have been observed in a variety of material systems, e.g. photoinduced superconductivity [1], structural modification of alloys [2], manipulation of topological phases in Weyl semimetals [3], vibrational dynamics following melting of atomic charge order in nickelates [4], hidden states during spontaneous symmetry breaking of charge density waves [5], and charge separation of chiral organic molecules [6]. Symmetry can also be manipulated in magnetic materials because of the interplay between

their local and nonlocal order parameters. Recent studies have indeed demonstrated that the homogeneously magnetized ferrimagnet GdFeCo undergoes phase-ordering kinetics through the ultrafast formation of localized defects [7]. Moreover, topological phases could be accessed in ferromagnetic materials biased with an external magnetic field, demonstrating the picosecond emergence and subsequent stabilization of skyrmion lattices [8], and in ferrimagnets showing the transition from helical to skyrmion phases [9]. In these works, the manipulation of symmetry occurred within the magnetic or spin degree of freedom. However, ultrafast excitation of metallic magnetic materials [10] also induces nonequilibrium spin currents [11] producing torques [12] that affect the picosecond dynamics of the spin degree of freedom [13–20], and phonon modes coupled to the magnetic system by magnetostriction to form nanosized spin-wave solitons [21].

A clear manifestation of spin-current-induced ultrafast magnetization dynamics is found in materials exhibiting

*Author to whom all correspondence should be addressed: eiacocca@uccs.edu

magnetization textures. It was recognized that materials stabilized in a stripe domain pattern could be demagnetized more quickly than the uniformly magnetized sample [17]. This finding provided an indication that the nonlocal magnetic texture affects the ultrafast behavior of the material. It is then natural to inquire how the different magnetic textures with distinct translation symmetries affect the picosecond magnetization dynamics, and how the textures themselves can be manipulated by optical excitations. Such control of magnetism at the femtosecond timescales is particularly important for proposals of energy-efficient and fast magnetic storage devices [22] where the information is encoded by magnetic domains along tracks, effectively imposing a randomized magnetic texture that should not be corrupted by external stimuli.

To study the far-from-equilibrium dynamics of magnetic textures occurring at the nanoscale, time-resolved x-ray scattering from free-electron lasers remains the preferred method to achieve the necessary combined temporal and spatial resolution [7,11,16,17,19,20,23]. The detected scattered intensity pattern directly correlates to the symmetry of the magnetization texture. Stripe domains exhibit spatial translation symmetry along one dimension, leading to a distinctive anisotropic scattering pattern. In contrast, labyrinth domains can be regarded as stripe domains where the underlying anisotropy is lifted, thus causing a randomized long-range order that gives rise to an isotropic scattering ring. This behavior is well-known in the broader field of pattern formation, particularly of Turing patterns [24]. In the context of x-ray Bragg diffraction, labyrinth domains would be similar to a polycrystalline or powder sample, which consists of randomly oriented crystallites (or grains) leading to the formation of well-known Debye rings. An extreme case is amorphous materials that have short-range order but no long-range order resulting in broad rings. On the other hand, stripe domains would be akin to diffraction from a single crystal, which exhibits spatial translation symmetry across the entire sample resulting in a Bragg spot.

Studies in both stripe and labyrinth domain patterns have provided a wealth of observations that to date remain disparate and controversial. Initial studies on labyrinth domains in Co/Pt multilayers reported a ring contraction of $\approx 4\%$ that was interpreted as a result of spin-current-induced domain-wall broadening [16]. This conjecture followed from the impossibility of a fractional expansion of the domain pattern, i.e., a change in periodicity in the probed section, that would imply domain-wall speeds over the speed of light. Later studies in CoFe/Ni multilayers that could access higher-order diffraction rings were able to disentangle domain-wall broadening from the spectral periodicity, demonstrating that the observed shift was related to nanoscopic variations in the domain pattern [20]. In particular, domain-wall broadening of 31% was identified from the relative harmonic amplitudes of the scattering rings, while the observed harmonic shift of 6% accompanied by a 15% linewidth broadening was consistent with domain-wall motion on the order of 2 km/s. More recently, a similar shift of $\approx 2.6\%$ in the scattered ring was observed for chiral labyrinth domains, which was explained by different demagnetization rates for homogeneous (domains) and inhomogeneous (domain-walls) regions of the sample [25]. Interestingly, this shift has not been observed

in stripe domains [17,19], contradicting earlier works that propose modifications of the domain-wall profile as the key effect. However, domain-wall broadening of 41% after 20 ps was clearly observed and attributed to a heat-induced reduction of the uniaxial magnetic anisotropy in Ref. [19].

We clarify these controversies by studying the time-resolved x-ray scattering from a magnetic multilayer sample which can exhibit stripe, labyrinth, and mixed domain characteristics. By isolating the different symmetries in the observed scattering pattern, we demonstrate symmetry-dependent ultrafast dynamics. In particular, only the isotropic component exhibits a shift of its peak position in reciprocal space, even when both symmetry components are present at the same time. This result alone conclusively proves that domain-wall broadening, which is presumably operative in both stripe and labyrinth samples, cannot explain the peak shift of the diffraction ring in labyrinth samples, as was previously proposed in Ref. [16].

For the mixed states, our data suggest that the recovery time for the isotropic and anisotropic components is different. Our studies indicate that the labyrinth magnetic textures are more prone to be spatially manipulated at ultrafast timescales and open new routes for the *spatial* ultrafast manipulation of magnetism.

II. EXPERIMENTAL METHODS

A. X-ray scattering measurements

Time-resolved small-angle x-ray scattering experiments (SAXS) were performed on CoFe/Ni multilayers grown on Si membranes at the European X-ray Free Electron Laser (EuXFEL). The magnetic multilayered samples with the stack layering of [Ta(3 nm)/Cu(5 nm)/[Co₉₀Fe₁₀(0.25 nm)/Ni(1.35 nm)] \times 8/Co₉₀Fe₁₀(0.25 nm)/Cu(5 nm)/Ta(3 nm)] were fabricated by sputter-deposition on polycrystalline Si membranes embedded in a Si substrate enabling x-ray transmission measurements [26]. Our multilayer composition informs that the saturation magnetization is $M_s = 616$ kA/m [26]. We have also measured damping to be $\alpha = 0.015$ and a g -factor of $g = 2.18$. Before the beamtime, MFM measurements showed the presence of out-of-plane labyrinth domains with an average size of 110 nm at remanence.

Figure 1(a) shows the pump-probe schematic of the experimental setup. The experiments are performed at the soft-x-ray coherent scattering (SCS) beamline at the EuXFEL [27]. The XFEL generates linearly polarized x-ray pulses with 25 fs duration. In this experiment, we use a pulse-to-pulse separation of 18 μ s, with 26 pulses per train, with the 468 μ s trains having a repetition rate of 10 Hz. This effectively results in 260 pulses per second impinging on the samples. While the EuXFEL is capable of a much higher pulse frequency with even more pulses per train, longer pulse trains with shorter pulse-to-pulse separation resulted in readily apparent sample damage. Even with these conditions, the sample is at an elevated temperature during the time-resolved measurements (see Appendix A). The incoming x-ray intensity (I_0) is monitored shot-by-shot using an x-ray gas monitor (XGM) [28].

The pump laser is synchronized with the FEL at half of the x-ray probe frequency to collect both the scattering data

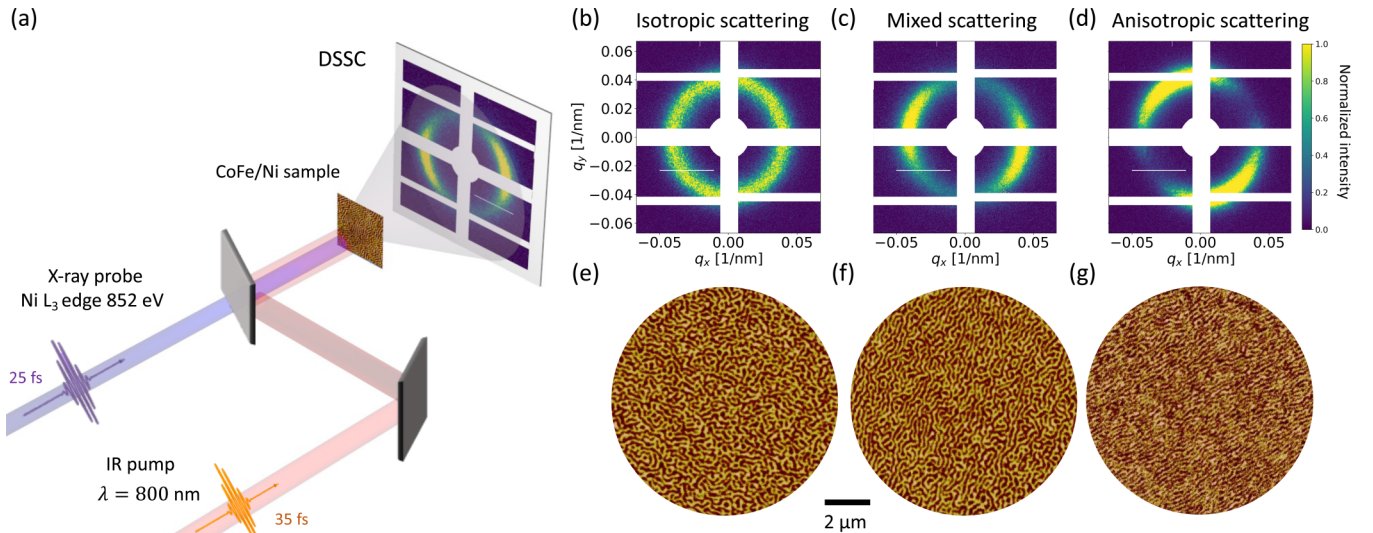


FIG. 1. (a) Schematic of the experimental pump-probe setup. The sample is excited by IR pulses and probed by linearly polarized x-rays tuned to the L_3 -edge of Ni. The scattered photons are collected on the DSSC detector. Representative diffraction patterns are shown for (b) labyrinth, (c) mixed, and (d) stripe domain patterns. All three patterns are found on the same sample membrane. Translation of the pump/probe beams across the sample allows access to different regions of the sample that exhibit the different scattering patterns. Corresponding $10 \times 10 \mu\text{m}^2$ MFM real-space images are shown in (e)–(g), illustrating the varying degree of randomness for each domain pattern.

from ultrafast dynamics (“pumped”) and in quasiequilibrium (“unpumped”) within the same measurement run. The x-ray scattering is collected on the DSSC 2D detector, able to match the repetition rate of the XFEL [29]. The DSSC records data at twice the x-ray pulse rate in order to collect so-called “dark” data frames in between pulses for the best background correction [30]. The sample to detector distance is fixed at 3 m. We note that the white regions in the scattering correspond to nonactive or faulty areas of the DSSC detector.

The samples are probed resonantly with linearly polarized x-rays tuned to the L_3 absorption edge of Ni (852 eV, 1.45 nm). The samples are pumped with a YAG-white-light-seeded laser with central wavelength $\lambda = 800$ nm and 35 fs pulse duration [31]. The x-ray spot size is estimated to be $20 \times 20 \mu\text{m}^2$, and the pump laser has a Gaussian profile with $40 \times 40 \mu\text{m}^2$ at full width at half-maximum. Magnetic domains act as a grating for x-rays at a resonant magnetic edge so that their scattering mathematically represents the two-dimensional Fourier transform of the grating [32]. By means of dichroic absorption and scattering [33,34], due to different cross-section of oppositely aligned up/down domains, small-angle x-ray scattering (SAXS) is collected on the DSSC 2D detector. For further information on resonant magnetic scattering, we refer the reader to Refs. [20,33,35,36].

Representative examples of static scattering patterns are shown in Figs. 1(b)–1(d). These data are collected within the same membrane but with the x-ray beam illuminating different areas of it. Each of these patterns illustrate distinct long-range symmetries present in the membrane which were characterized in real space after the pump-probe experiments using magnetic force microscopy (MFM) as shown in panels (e)–(g). The isotropic ring (b) results from labyrinth domains (e) while the anisotropic, lobed pattern (d) results from domains with a similar translation symmetry to stripe domains

(g). We also observe a “mixed” state where both symmetry features are visible in the scattering (c). The corresponding MFM image (f) indicates that this pattern arises from a varying degree of randomness in the spatial periodicity of the domain structure. In other words, the preferentially labyrinth and striped areas are spatially intermixed rather than clustered.

We note that we do not use an external in-plane field to induce a striplike domain pattern [17,19,32], but instead we find this preferential orientation in sample areas that are subject to strain. As further elaborated on in Appendix B, this strain is the result of irreversible and slow plastic deformation due to sample heating that occurred during the course of the experiment.

B. Data analysis method

Traditionally, time-dependent 2D scattering has been analyzed within a 1D representation achieved by azimuthal integration, either over the isotropic ring [16,20,25,37] or the anisotropic lobes [17,19]. However, this simple analysis hides valuable spatial information obtained by scattering experiments. In particular, our scattering data exhibit mixed isotropic-anisotropic scattering, and a significant amount of data are lost to the nonactive regions of the detector. For example, azimuthal averaging of the data results in the apparent development of a bimodal distribution due to missing pixels, discussed in Appendix C. Such artifacts can result in an erroneous quantification of the far-from-equilibrium physics at play. For these reasons, we developed a 2D fitting procedure that accurately models the varying degree of domain symmetry in our samples and allows us to reconstruct the full scattering pattern, therefore providing an accurate picture of the far-from-equilibrium magnetization dynamics in our samples.

Motivated by the MFM images, we utilize a fitting function for the scattered intensity given by

$$I(\mathbf{q}, \varphi) = I_0 + I_{\text{iso}}(\mathbf{q}) + I_{\text{aniso}}(\mathbf{q}, \varphi), \quad (1)$$

where \mathbf{q} is the wave vector, φ is the azimuthal angle at which the anisotropic lobes are oriented, I_0 is a uniform background, $I_{\text{iso}}(\mathbf{q})$ is the isotropic component that is a function of the wave vector, and $I_{\text{aniso}}(\mathbf{q}, \varphi)$ is the anisotropic component which is a function of both the wave vector and the azimuthal angle. The scattered intensities are proportional to the modulus square of the magnetic scattering amplitude resulting from the magnetic texture. Because intensities are photon counts, the square root of the intensity is a measure of the relative contrast due to the amplitude of the magnetization modulus within the magnetic texture.

We mathematically assume that both scattering patterns arise from an intermixed spatial pattern, resulting in no coherent interference contribution to the scattering, as elaborated on in Appendix D. This implies that the domain patterns exhibit a highly varying spatial periodicity that precludes any possibility of long-range phase coherence of the resultant scattering, in agreement with the MFM images of Figs. 1(e)–1(g).

Based on previous works [7,20], we define the isotropic scattering intensity as

$$I_{\text{iso}}(\mathbf{q}) = \left[\frac{A_0}{(\mathbf{q} - q_0)^2 / \Gamma_0^2 + 1} \right]^2, \quad (2)$$

where A_0 is the amplitude, q_0 is the radius of the isotropic peak position, and Γ_0 is the linewidth.

The anisotropic scattering can be phenomenologically represented by a Fourier series $\sum A_n \sin^2(n(\varphi - \theta))$. The intensity is thus defined to second order as

$$I_{\text{aniso}}(\mathbf{q}, \varphi) = \left[\frac{|A_1| \sin^2(\varphi - \theta) + A_2 \sin^2(2(\varphi - \theta))}{(\mathbf{q} - q_1)^2 / \Gamma_1^2 + 1} \right]^2. \quad (3)$$

This functional form considers that the anisotropic scattering is aligned at an angle θ , has an anisotropic peak position q_1 , and has a linewidth Γ_1 . The two amplitude coefficients correspond to the dominant scattering amplitude A_1 and a deviation from a sinusoidal azimuthal profile, A_2 . We find that A_2 is typically two orders of magnitude smaller than A_1 .

Fitting a 2D function with eight fitting parameters requires a detailed and robust protocol. We utilize the following procedure: (i) the center of the scattering intensity $\mathbf{q} = \mathbf{0}$ is determined at the beginning of each run. Indeed, even a one-pixel offset of the center can generate artefacts such as asymmetries in the radial peak position. For this reason, the correct determination of $\mathbf{q} = \mathbf{0}$ is critical. (ii) The anisotropic component alignment θ is determined. (iii) The fitting parameters are included sequentially with the goal of determining a good initial guess in an automated way. (iv) Fitting of Eq. (1) is performed with all eight parameters adjustable. By use of this procedure, we obtain high-fidelity fits with small and spatially randomized residuals, discussed in Appendix C. From the fitted parameters, we focus on the magnetization quench and the radial peak position of each component. The average magnetization for each symmetry component is proportional to the amplitudes A_0 and A_1 , insofar as $A_2 \ll A_1$ for the

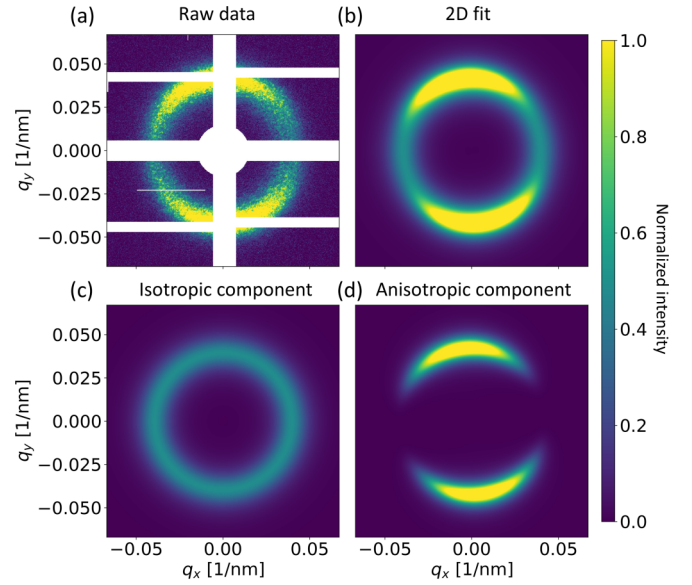


FIG. 2. Two-dimensional fit of the scattering data. (a) The raw experimental data suffer from missing intensity in the nonactive regions of the DSSC. (b) Two-dimensional fit with Eq. (1). The fit allows us to fully separate the (c) isotropic and (d) anisotropic components of the scattering.

anisotropic component. The peak position is directly obtained from the fitted parameters q_0 and q_1 .

An example of a 2D scattering fit using Eq. (1) is shown in Fig. 2. The raw experimental scattering in (a) exhibits features obstructed by the inactive areas of the detector. The 2D fit reconstruction is shown in (b), clearly reproducing the main features of the scattering and allowing us to separate the isotropic and anisotropic components, shown in (c) and (d), respectively. It is interesting to note that the anisotropic component alignment θ was found to depend on the probe's position on the sample but remained constant throughout the pump-probe experiment within our fitting accuracy of 1 degree. This indicates that long-range order of the anisotropic component is maintained upon ultrafast pumping.

Based on our fits, we estimate the number of photons contributing to each symmetry component in the scattering to classify them as isotropic, anisotropic, or mixed. We use the following ratio of scattered photons:

$$\text{ratio} = \frac{\text{isotropic photons} - \text{anisotropic photons}}{\text{total photons}}. \quad (4)$$

Considering that the background always contributes with a finite amount of photons, isotropic scattering has a ratio close to 1 while anisotropic scattering has a ratio close to -1 . For a ratio between -0.3 and 0.9 we classify the scattering pattern as a mixed state. The full analysis on our data is further described in Appendix E. Based on the photon-count classification, we analyze the ultrafast evolution of the average magnetization, proportional to the fitted amplitude, and the peak position for isotropic and anisotropic scattering patterns. The temporal evolution of both quantities is fitted by the

double-exponential function

$$f_{\text{quench}} = (1 + B - A) + Ae^{-(t-t_0)/\tau_m} - Be^{-(t-t_0)/\tau_R}, \quad (5)$$

where t_0 is the time zero of the dynamics, τ_m is the quench constant, τ_R is the recovery constant, and A and B are dimensionless constants related to the quench and recovery of the magnetization. A more complete form of this equation was derived in Ref. [38]. Here, we use a simplified form that disregards the longer algebraic recovery constant that could not be fitted accurately within the 20 ps traces. From this equation, we can obtain the quench time t_{min} and the maximum quench of the magnetization $\Delta M/M$ as derived parameters from the fitted variables. Further details on how to obtain such variables and their errors are given in the Appendix F. The quantities extracted from the fits are summarized in Table I.

III. ULTRAFAST MAGNETIZATION DYNAMICS

The normalized modulus of the magnetic diffraction amplitude at $t < 0$ is shown in Fig. 3(a) for isotropic scattering patterns, and Fig. 3(b) for anisotropic scattering patterns. We observe a similar amount of quenching for both types of scattering using the same fluence. In particular, we determine $38.5 \pm 0.8\%$ and $37.6 \pm 0.4\%$ for the isotropic and anisotropic components, respectively. The solid gray curves in Fig. 3(a) correspond to the unpumped data and serve to confirm the negligible evolution of the magnetization in a quasiequilibrium state. It is worth pointing out that the samples do not return to thermal equilibrium at the repetition rate of the experiment, as further discussed in Appendix A. We also studied the fluence dependence and relative position between the pump and the probe, labeled as FO (full overlap) and PO (partial overlap, shifted by 50 μm) in Table I. We discuss this dependence in Sec. IV. The effect of pump fluence was investigated and found to be in agreement with previous works [14,16,17,39–41]. These results are shown in Appendix G and further validate the 2D fitting approach.

In addition to the quench, we also detect an ultrafast contraction of the ring radius of $0.84 \pm 0.06\%$ for the isotropic component, shown in Fig. 3(c). On the contrary, we do not observe conclusive evidence of a peak position shift for the anisotropic scattering, as shown in Fig. 3(d). While it can be argued that a small shift of 0.5% is apparent, we cannot conclusively quantify this shift within our signal-to-noise ratio. In addition, other data sets do not exhibit any apparent shift, as shown in Table I.

These observations are consistent with previous works where a shift in the radial wave vector \mathbf{q} was only observed when measuring isotropic scattering from labyrinth domains [16,20,25] and no shift reported for anisotropic scattering from stripe domains [17,19]. We note that the detected shifts (1–4 %) are smaller than those observed in earlier works (5–6 %) [16,20]. This difference in our data relative to earlier reports could be a consequence of the lower fluences and/or the elevated temperature of our samples due to the large effective repetition rate of the instrument (see Appendix A). An elevated temperature before time zero reduces the local magnetic moment such that the net electron-spin scattering that drives the magnetization dynamics is weaker. Regardless, we conclude based on our analysis of the isotropic and anisotropic

TABLE I. Extracted parameters from the 2D and temporal double-exponential fits. Measurements are listed by pump fluence and scattering pattern. We distinguish between full overlap (FO) and partial overlap (PO) between pump and probe. We report the extracted domain size π/q_1 (nm) from the prepumped signal, maximum shift in radial peak position (%), maximum demagnetization (%), and demagnetization recovery time (ps) for all measurements.

Run ID	Fluence	SAXS pattern	Isotropic component						Anisotropic component							
			Prepumped			Pumped			Prepumped			Pumped				
			size (nm)	$\Delta q_0/q_0$ (%)	$\Delta M/M$ (%)	t_{min} (ps)	τ_R (ps)	size (nm)	$\Delta q_1/q_1$ (%)	$\Delta M/M$ (%)	t_{min} (ps)	τ_R (ps)	size (nm)	$\Delta q_1/q_1$ (%)	$\Delta M/M$ (%)	t_{min} (ps)
1	20 mJ cm ⁻²	FO (day 3)	78.30 ± 0.11	1.0 ± 0.4	43.5 ± 0.9	0.714 ± 0.033	3.16 ± 0.27	74.55 ± 0.04	0	35.4 ± 1.0	0.592 ± 0.003	2.25 ± 0.14				
2	15 mJ cm ⁻²	FO (day 3)	77.27 ± 0.14	1.5 ± 0.6	29.3 ± 1.0	0.660 ± 0.039	2.80 ± 0.23	73.58 ± 0.04	0	20.9 ± 1.4	0.549 ± 0.043	1.52 ± 0.14				
3	25 mJ cm ⁻²	FO (day 4)	71.96 ± 0.34	3.5 ± 2.3	38.2 ± 1.4	0.970 ± 0.049	2.05 ± 0.17	74.06 ± 0.14	0.5 ± 0.5	34.9 ± 1.8	0.836 ± 0.049	1.68 ± 0.15				
4	15 mJ cm ⁻²	FO (day 4)	71.86 ± 0.28	2.7 ± 2.7	21.2 ± 1.0	0.738 ± 0.012	1.73 ± 0.18	74.98 ± 0.14	0	18.0 ± 1.8	0.679 ± 0.021	0.99 ± 0.15				
5	15 mJ cm ⁻²	FO (day 5)						73.08 ± 0.01	0	56.7 ± 0.7	0.58 ± 0.02	2.86 ± 0.08				
6	15 mJ cm ⁻²	PO (day 5)	77.56 ± 0.04	1.88 ± 0.07	21.9 ± 0.7	0.610 ± 0.02	1.29 ± 0.07	74.16 ± 0.03	0.23 ± 0.05	24.1 ± 0.2	0.61 ± 0.02	1.04 ± 0.05				
7	10 mJ cm ⁻²	PO (day 5)	89.38 ± 0.02	0.70 ± 0.05	12.6 ± 0.5	0.840 ± 0.02	0.87 ± 0.05									
8	10 mJ cm ⁻²	FO (day 5)	76.66 ± 0.01	0.84 ± 0.06	38.5 ± 0.8	0.964 ± 0.02	1.57 ± 0.03									
9	10 mJ cm ⁻²	FO (day 5)						72.3 ± 0.01	0	37.6 ± 0.4	0.813 ± 0.013	1.65 ± 0.02				

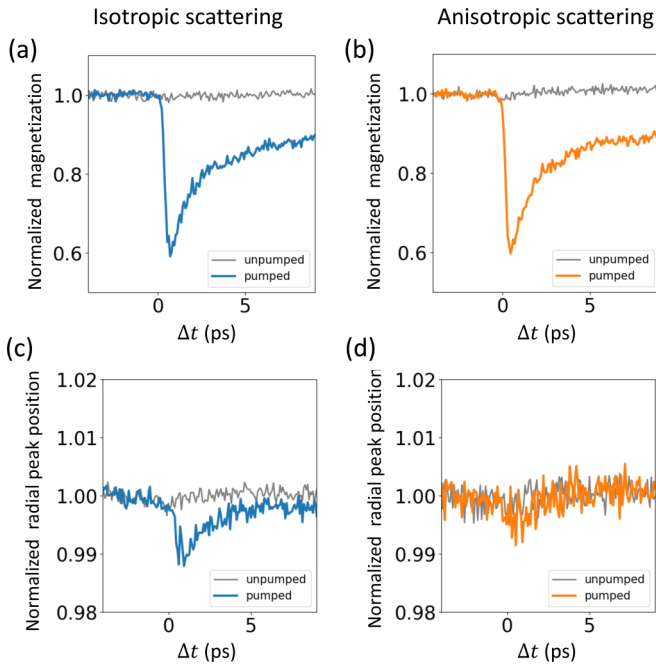


FIG. 3. Two-dimensional fitting of the full diffraction pattern is used to extract the time traces of both the magnetization and the peak position for the isotropic and anisotropic scattering patterns with 10 mJ cm^{-2} FO pump fluence (runs 8 and 9 in Table I, respectively). The normalized magnetization of isotropic and anisotropic scattering patterns is shown in (a) and (b), respectively. The magnetization is shown by the solid colored curves and corresponding unpumped data by solid gray curves. In both cases, the amount of quenching is similar. The corresponding time traces for the scattering peak position are shown in (c) and (d) for the isotropic and anisotropic scattering patterns, respectively, by colored solid curves. The gray solid curves corresponds to the unpumped scattering peak position in quasiequilibrium. Only the isotropic component exhibits a significant peak shift estimated to $0.84 \pm 0.06\%$. The peak shift of the anisotropic component, while noticeable by eye in Fig. 3(d), is not statistically significant to within error bars. The shaded area in all cases corresponds to the standard deviation of the fitted quantities. Because of the high accuracy in the fitting for each time instance, the standard deviation of the fitted variables is not visible to the eye. Noise is instead dominated by measurement fluctuations.

scattering that the difference in the shifts in \mathbf{q} for stripe and labyrinth domains is not related to varying sample properties or experimental details since our measurements are obtained from the same sample and experiment.

To investigate this further, we turn to the mixed scattering patterns where both isotropic and anisotropic contributions exhibit a similar photon count. A representative example is shown in Fig. 4 for the time-dependent magnetization [(a) and (b)] and peak shift [(c) and (d)] of the isotropic (blue) and anisotropic (orange) components, respectively. As in Fig. 3, the solid gray curves represent the unpumped data. We note that the signal-to-noise ratio of the mixed states is lower than that of pure states, but the main features can be recovered from the 2D fits with good accuracy. There are two main observations from Fig. 4. First, the quench of both symmetry components is similar, estimated to be $38.2 \pm 1.4\%$ and $34.9 \pm 1.8\%$ for the isotropic and anisotropic components, re-

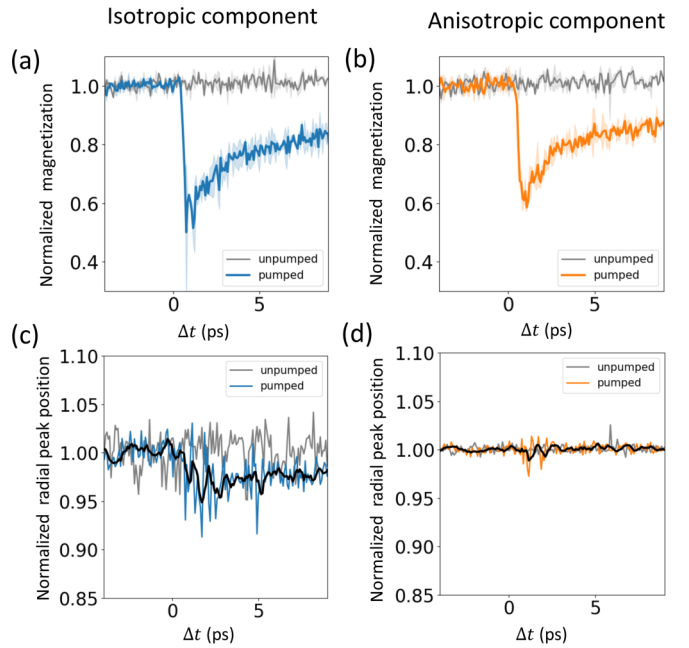


FIG. 4. Two-dimensional fitting results for the mixed state diffraction pattern with 25 mJ cm^{-2} pump fluence (run 3 in Table I). The time traces of both the magnetization and the radial peak position for the isotropic and anisotropic components are extracted from fitting the full diffraction pattern. In all panels, the gray curves represent the unpumped data. The normalized magnetization of isotropic and anisotropic components is shown in (a) and (b), respectively. We observe a similar amount of quenching in both cases. The scattering peak position is shown in (c) and (d) for the isotropic and anisotropic components, respectively. Only the isotropic component of the mixed SAXS pattern exhibits a significant shift in the radial peak position. This is similar to what was found for the purely isotropic or purely anisotropic SAXS scattering patterns, where only data with purely isotropic scattering exhibited significant radial peak shifts. Here we detect a shift of $3.5 \pm 2.3\%$. The black curve is the five-point moving average of the data. The shaded area corresponds to the standard deviation of the fitted quantities.

spectively. Second, there is a distinct shift in the peak position of the isotropic component, while no shift can be conclusively detected from the anisotropic component. The same trend is observed in all the mixed scattering patterns measured and analyzed, as summarized in Table I. Notably, the ultrafast shift of the isotropic component is consistently larger than any shift in the anisotropic component.

Our observation of a peak shift only, or at least predominantly, for the isotropic ring suggests either a systematic effect arising from modification of x-ray scattering or a symmetry-dependent effect arising from the magnetic order itself. Modification of x-ray scattering, whereby ultrafast domain-wall broadening could lead to an apparent shift in the scattering ring, was proposed in Ref. [16]. This approach is analogous to invoking a nonequilibrium Debye-Waller factor that mimics thermal fluctuations in crystal lattices. This approach was largely disproved in Ref. [20] based on the simultaneous quantification of domain-wall broadening and peak shifts.

While our current experiments have limited dynamic range compared to previous works [19,20], our two-dimensional experimental results based on the first-order scattering can further demonstrate that invoking a Debye-Waller-like factor in this context is not appropriate. Under the assumption that such a factor originates from a stochastic effect, it stands to reason that it must be isotropic in \mathbf{q} , with a characteristic form $e^{-|\mathbf{q}|^2/2\sigma^2}$ [42]. In Ref. [20], a relationship between $\sigma(t)$ and the measured linewidth Γ and equilibrium domain size q was obtained, and it can be algebraically manipulated as

$$\frac{\Delta q}{q} = \frac{\Gamma^2}{2\sigma^2 + \Gamma^2}. \quad (6)$$

From this formula, we find two relevant limits. If σ is small, the attenuation results in $\Delta q/q \approx 1$ for both isotropic and anisotropic components. This effectively implies a case in which the scattering is fully attenuated and instead dominated by thermal vibrations. In the limit of $\sigma > \Gamma$, which represents the experimental condition by which thermal vibrations are shorter than the domain-pattern correlation length, then $\Delta q/q \propto \Gamma^2$. Consequently, the ratio between the anisotropic and isotropic shifts should be proportional to Γ_1^2/Γ_0^2 . From our data analysis (see Tables IV and V), we find that the squared linewidth ratio is ≈ 0.25 in all cases. This relative shift was not observed even though our experimental data provided such accuracy. For example, the mixed state pumped at 15 mJ/cm² in partial overlap (run 6 in Table I) was found to exhibit a $\Delta q/q$ of 1.88 ± 0.07 and 0.23 ± 0.05 for the isotropic and anisotropic components, respectively. The prediction based solely on the Debye-Waller factor suggests instead an isotropic shift of 0.72 ± 0.03 , well within accuracy. Therefore, the argument of an attenuation factor producing an apparent shift in the scattering fails to explain our observations.

Summarizing this section, we studied the time-dependent ultrafast response of a magnetic sample with different domain patterns with distinct translation symmetry. In cases in which the quenching was similar, we observe a shift in the scattering peak position only for the isotropic component for both the preferential labyrinth domain and the mixed state. Our attempt to fit the observed peak shift with a Gaussian Debye-Waller factor (DWF), ostensibly capturing spectral attenuation effects due to domain-wall broadening, was not successful. The failure of this model stems from a significant quantitative mismatch between the observed peak shift and broadening of the diffraction ring: If we attribute the ring broadening to a DWF, then the amount of peak shift that we observe is actually ≈ 3 times smaller than expected. Instead, this experimental observation is consistent with a symmetry-dependent effect arising from the magnetic order itself.

IV. DISCUSSION

The main observation of our work is the unequivocal shift in the isotropic component of the scattering, even when simultaneously observed with an anisotropic component. We substantiate this statement by statistical analysis of the fitted parameters presented in Table I. We use weighted averages and weighted standard deviations to minimize the impact of data points determined with lower accuracy. An average peak

shift of $1.09 \pm 0.51\%$ for the isotropic component was calculated. We emphasize that this statistically significant peak shift is a general behavior and thus independent of the particular fluence conditions, day of the experiment, and regions illuminated. Contrarily, an average peak shift of $0.22 \pm 0.22\%$ was found for the anisotropic component. This means that the peak shift in the anisotropic component is statistically insignificant within the signal-to-noise ratio of the measurement.

Our data analysis procedure also allows us to extract information on the quench time, t_{\min} , and recovery time constant, τ_R , for each scattering component. The average quench time was determined to be 0.78 ± 0.11 and 0.70 ± 0.10 ps for the isotropic and anisotropic components, respectively. This is a clear indication that the quench time is independent of the symmetry component. Magnetic quench occurs in textured magnetic materials due to both the increase of the magnon population and domain-wall broadening. Therefore, the similar quench time is in agreement with the notion that ultrafast demagnetization occurs at the atomic scale, driven by the coupling between light and electrons at femtosecond timescales. It was found that the recovery time constant τ_R scales linearly with quench amplitude $\Delta M/M$ for both the isotropic and anisotropic components of the diffraction ring. We consider a recovery speed from a weighted linear fit of the recovery time constant and the quench amplitude, where the recovery rate is defined as $d(\Delta M/M)/d(\tau_R)$. This allows us to compare the overall dependence of τ_R on quenching for both components of diffraction when they have different quench amplitudes. The average reciprocal recovery speeds were determined to be 5.2 ± 0.8 and 4.8 ± 0.3 ps for the isotropic and anisotropic components, respectively. As for the quench time, the recovery constant is statistically indistinguishable for both cases.

A microscopic mechanism explaining the observed behavior is still lacking. Numerical modeling is challenging because reasonably large magnetic volumes are required to stabilize magnetic domains and are currently only accessible with micromagnetic models. As shown elsewhere, micromagnetic models are not appropriate to model the ultrafast increase in the magnon thermal population, specifically for short-wavelength magnons [7], but progress is being made from the point of view of Landau-Lifshitz-Bloch models [43]. In addition, theoretical models are presently constrained to macroscopic averages [44] and superdiffusive spin currents [12,45]. Therefore, we can only conjecture based on the experimental data.

The presented results strongly suggest that regions of the sample with domains preferentially parallel to one another are effectively inert to spatial modification. Conversely, regions of the sample with disordered domains can be spatially modified. Considering that the domain sizes are on the order of 80 nm, this effect must be localized within the domain walls, which are the only objects in the system capable of exchanging information between neighboring domains. We speculate that torque exerted from angular momentum is a possible mechanism acting on the domain walls in the form of, e.g., superdiffusive spin currents [12] or magnons with wavelengths under 100 nm. It would also be interesting to consider the possibility of spin-wave dispersive shock waves [46] that have been numerically [47–51] and experimentally [52] observed in magnetic materials. While these mechanisms

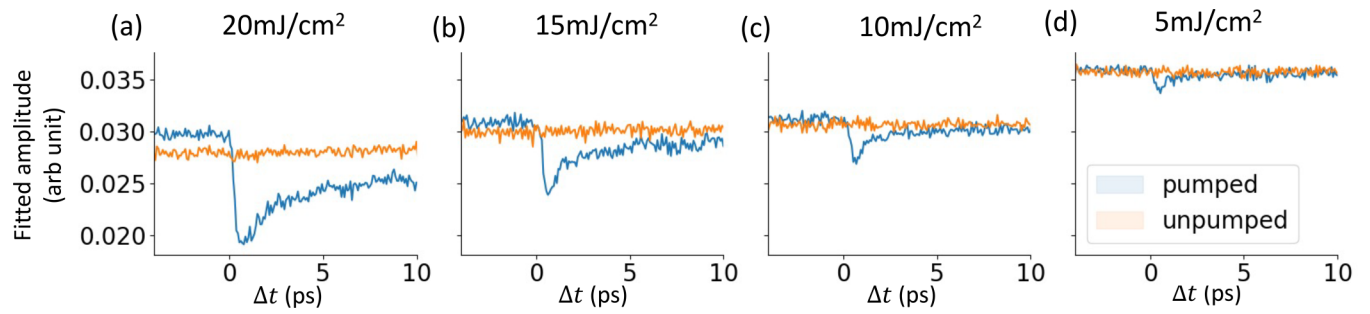


FIG. 5. Fitted lobe amplitude for a series of pump-fluences (a) 20 mJ cm^{-2} , (b) 15 mJ cm^{-2} , (c) 10 mJ cm^{-2} , and (d) 5 mJ cm^{-2} . We observe an offset between the pumped (blue) and unpumped (orange) data before $\Delta t \leq 0$ attributed to the data not having fully returned to equilibrium between pulses.

remain to be demonstrated, it would be interesting to consider them in future studies in a far-from-equilibrium regime.

V. CONCLUSION

We reveal the dependence of the ultrafast spin dynamics on the nanoscale configuration of magnetic domains. Our results dispel the apparent inconsistency of previously reported values for the radial peak shift after ultrafast pumping, given that all the presented data were taken with (i) the same sample, (ii) in the same manner, and (iii) at the same facility. We now clarify that the previous inconsistency in detection of the peak shift is because significant shift only occurs in samples with labyrinth domain patterns, characterized by an isotropic SAXS scattering ring. Moreover, our results strongly suggest that this behavior is intrinsically related to the magnetization textures and their symmetries. Surprisingly, these distinct dynamics arise from the symmetry of long-range-ordered magnetic domains with sizes ranging between 70 and 90 nm, and extending for several microns, both dimensions longer than the typical mean free path of electrons in metallic multilayers [34].

The mechanism of the observed shift is still debatable. While a uniform domain expansion can be excluded by impossibly large domain-wall motion speeds [16], it remains plausible that domains spatially rearrange [20] or locally demagnetize at different rates. Our results invite further experimental and theoretical research to clarify the impact of symmetries on the transfer of angular momentum between the electronic and spin degrees of freedom for far-from-equilibrium phenomena. In particular, the possible excitation of short-wavelength spin waves from the domain walls could be envisioned as a mechanism to exchange angular momentum [53] between domains and exert torque [12] on domain walls.

The raw data generated at the European XFEL are available [54].

ACKNOWLEDGMENTS

The authors acknowledge the European XFEL in Schenefeld, Germany, for provision of X-ray Free-Electron Laser beamtime at Scientific Instrument SCS, and we thank the instrument group and facility staff for their assistance. The authors thank Andrea Castoldi (DSSC consortium) for con-

tributing to the generation of DSSC gain files, and Carsten Deiter for the confocal microscopy images. R.J., M.M., and R.K. acknowledge support from AFOSR Grant No. FA9550-19-1-0019. D.T. and H.A.D. acknowledge support from the Swedish Research Council (VR), A.H.R. acknowledges support from the U.S. Department of Energy, Office of Science, Office of Basic Energy Sciences under Contract No. DE-AC02-76SF00515. N.Z.H. and S.B. acknowledge support from the European Research Council, Starting Grant No. 715452 MAGNETIC-SPEED-LIMIT. E.I. acknowledges the College of Letters, Arts and Sciences at UCCS for start-up support.

APPENDIX A: HEATING IN SAMPLES DUE TO HIGH REPETITION RATE

The EuXFEL can achieve MHz repetition rates with the SCS beamline being able to deliver up to 150 x-ray pulses per train. However, we observed that a higher repetition rate and shorter pulse-to-pulse separation lead to visible damage in our samples.

Our pumped-probe measurements were performed with 26 x-ray pulses per train at a pulse rate of 56 kHz and 13 IR pulses at half this rate. Within one measurement, we record both a pumped and an unpumped signal separated by $18 \mu\text{s}$. While we observe no apparent damage in the unpumped signal, we do observe an offset before time-zero in the fitted amplitudes of pumped and unpumped signals. Figure 5 shows that this offset increases with pump fluence. We conclude that $18 \mu\text{s}$ was not long enough for our samples to fully thermalize and return to equilibrium. We therefore have to keep in mind that our samples were at an elevated temperature, which could explain why the effects we observed are less pronounced than other measurements performed at different free-electron facilities that run at considerably lower repetition rate (50 and 120 Hz at FERMI and LCLS, respectively).

APPENDIX B: STRAIN IN MULTILAYERS

The magnetic multilayers were deposited on polycrystalline Si membranes. The measured membranes were characterized post-beamtime using confocal microscopy and magnetic force microscopy (MFM). From the confocal microscopy image Fig. 6(a) we observe that the x-rays and IR laser left *imprints* of up to 75 nm in the membranes. The

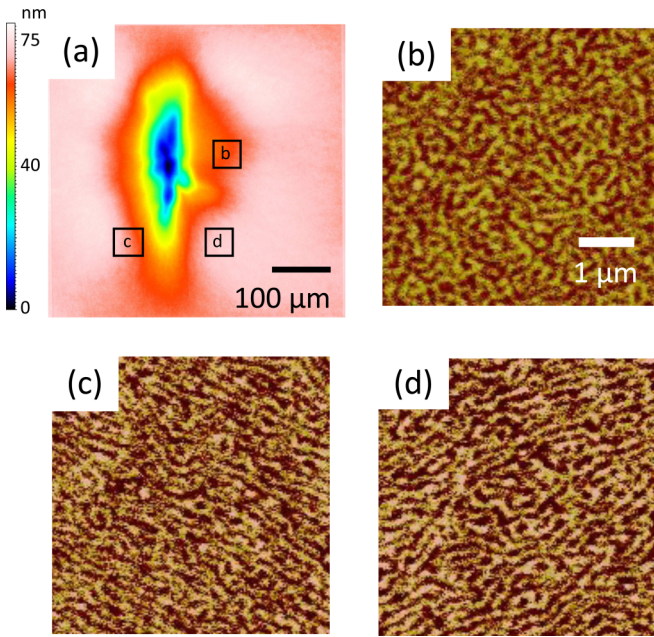


FIG. 6. (a) Confocal microscope image of a membrane after x-ray and IR laser exposure. MFM measurements were performed on the membrane after the beamtime. $5 \times 5 \mu\text{m}^2$ images taken at different areas of the membranes are showing (b) labyrinth domains, (c) partially oriented domains, and (d) partially oriented along the opposite direction.

strain near this distortion of the sample would explain why we observed anisotropy in the scattering pattern. Indeed, the MFM measurements confirm that the domains were oriented differently throughout the sample with some areas presenting labyrinth domains [see Fig. 6(b)], while others showed partially oriented domains at different angles [see Figs. 6(c) and 6(d)].

The dimpling of the membrane results from thermally induced buckling during the pulse train utilized at the Eu-XFEL. The pulse trains are 0.5 ms in duration, with 26 pulses in each train. As such, the time interval between each pulse in the pulse train is insufficient to achieve thermal relaxation. Estimating an optical absorption coefficient of 10%, we obtain a temperature gradient across the sample of approximately 100 K. Assuming a thermal expansion coefficient of 10^{-5}

$1/C$, the strain would be on the order of 0.1% at the elevated thermal equilibrium.

APPENDIX C: 2D FITTING PROCEDURES AND QUALITY ESTIMATION

We highlight the importance of fitting the center of the scattering data instead of relying on the center of the raw image from the DSSC. For example, we consider the scattering data shown in Fig. 7(a). Taking $\mathbf{q} = \mathbf{0}$ as the center of the scattering intensity, we azimuthally integrate the left and right modules of the scattering. As a result, we observe in Fig. 7(b) that the azimuthal profiles of the left and right features do not fully overlap at the same wave number. This is not physical because the lobe pattern must be mirror symmetric about the origin. By including the center of the scattering as a fitting parameter, we are able to determine the true $\mathbf{q} = \mathbf{0}$ as a function of pixels in the DSSC detector. The azimuthal profile of the features then overlaps perfectly as shown in Fig. 7(c). We find that the offset is typically within 2 pixels, which is less than 0.5 mm. We keep the center as a floating parameter when fitting the time-resolved measurements.

Another important aspect of the data analysis is found in the inactive areas of the DSSC detector, that sometimes cover substantial parts of the diffraction pattern as seen in Fig. 8(a). The 2D fit extrapolates the intensity in areas with missing pixels and allows us to reconstruct the full scattering, as shown in Fig. 8(b).

A natural question is whether this reconstruction is accurate and physically meaningful. An effective means of testing the importance of our 2D fitting procedure is to compare the azimuthal averages of both the raw data, Fig. 8(a), and the full 2D fitting function, Fig. 8(b). The comparison is shown in Fig. 8(d), where the averaged raw data are represented by the solid green curve, and the averaged full fit is represented by the dotted blue curve. Since the raw data span a substantial fraction of the DSSC detector without any active pixels, it is not surprising that the azimuthal averages of the raw data and the full 2D fitting function, which analytically accounts for the missing pixels, would exhibit very different azimuthal averages. If we take the full 2D fitting function and mask out the detector area that does not have any active pixels, Fig. 8(c), before performing an azimuthal average (orange dotted curve), we find that the azimuthal averages of the raw data and the

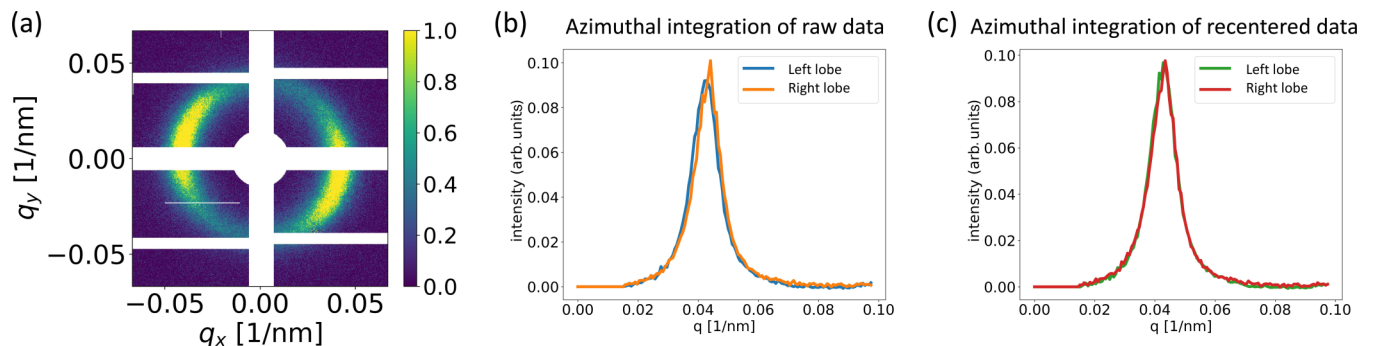


FIG. 7. (a) The raw data collected on the DSSC. The azimuthal integration over the top left and bottom right lobes is plotted for the raw image (b) and for the recentered image (c). The recentered image has been shifted by +0.7 pixels in x and +1.8 pixels in y .

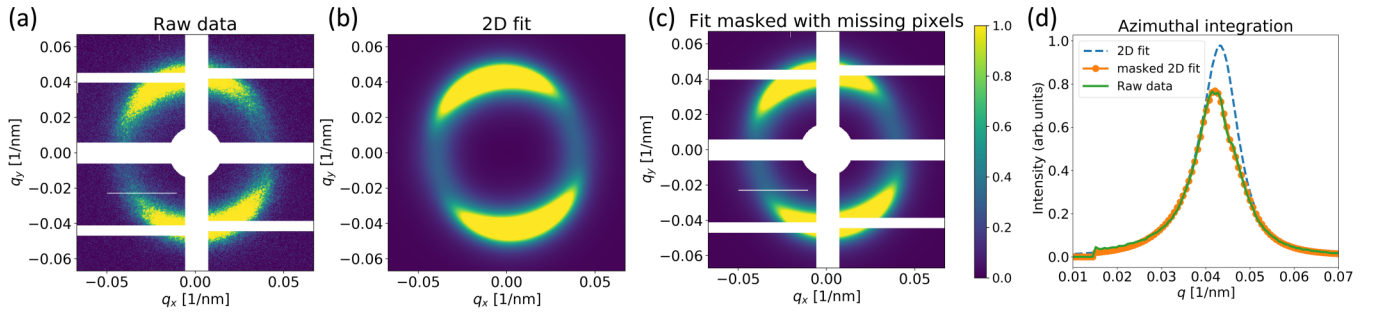


FIG. 8. (a) The raw scattering collected on the DSSC. (b) The result of the 2D fit. (c) 2D fit masked with the inactive areas of the detector. (d) Azimuthally integrated scattering of the raw data (solid green curve), 2D fit (dashed blue curve), and masked 2D fit (dotted orange curve). The 2D fit only matches the raw data once they have been masked with the DSSC inactive areas.

masked 2D fit are nearly identical. But we also see that both these azimuthal averages exhibit an artificial shoulder at $q \approx 0.045 \text{ nm}^{-1}$ that suggests a bimodal distribution. On the other hand, the anomalous shoulder is no longer present when we azimuthally integrate the fitted 2D function for the diffraction. In other words, azimuthal integration/averaging of raw SAXS scattering data that span large portions of a detector without active pixels can easily introduce artifacts that are eliminated when performing a proper fit with our continuous 2D fitting function.

This shows that the intensity mismatch, asymmetry, and shoulder in the raw data are only due to the inactive areas of the DSSC, and it indicates that great care must be taken when extracting information from azimuthally averaged or integrated data from a modular DSSC. These artefacts can suggest nonexistent physics in the ultrafast regime.

The quality of the fit is determined from the residual between the raw data and the fit. In Fig. 9 we show an example scattering pattern, its fit, and the residual. There is a clear finite residue at the location of the ring that indicates that our phenomenological function fails to correctly account for the detailed scattering profile. However, the residual is on the order of 10%. In addition, the residual fluctuates rapidly, which can also be a consequence of shot noise, proportional to the intensity, and the speckle pattern. We then conclude that our fits are sufficiently accurate to extract physically meaningful information.

We further validate our results by showing that the 2D fit is able to track small changes in the anisotropic peak position q_1 . We generate a mock scattering pattern with added shot noise, shown in Fig. 10(a), and a shift in q_1 of approximately 1%. The shift in q_1 is recovered by the fitting procedure within error. The parameters are given in Table II. The residual Fig. 10(b) shows the difference between the mock data and the fit. There is a clear residue with fluctuating values due to the shot noise of the mock data.

APPENDIX D: ABSENCE OF COHERENT INTERFERENCE IN THE SCATTERING PATTERN

We demonstrate that the fitting function for the diffraction pattern can be approximated by the addition of two intensities without any cross-correlation. For simplicity, we consider a 1D model with regions of spatial width a , each with a phase ϕ and a periodicity q_n . The 1D real space function f_1 can be expressed as an infinite sum of such regions, given by

$$f_1(x) = \sum_n^{\infty} \sin(q_n x + \phi_n) \Pi((x + n/2)/a), \quad (\text{D1})$$

where $\Pi(x/a)$ is the pulse function of width a .

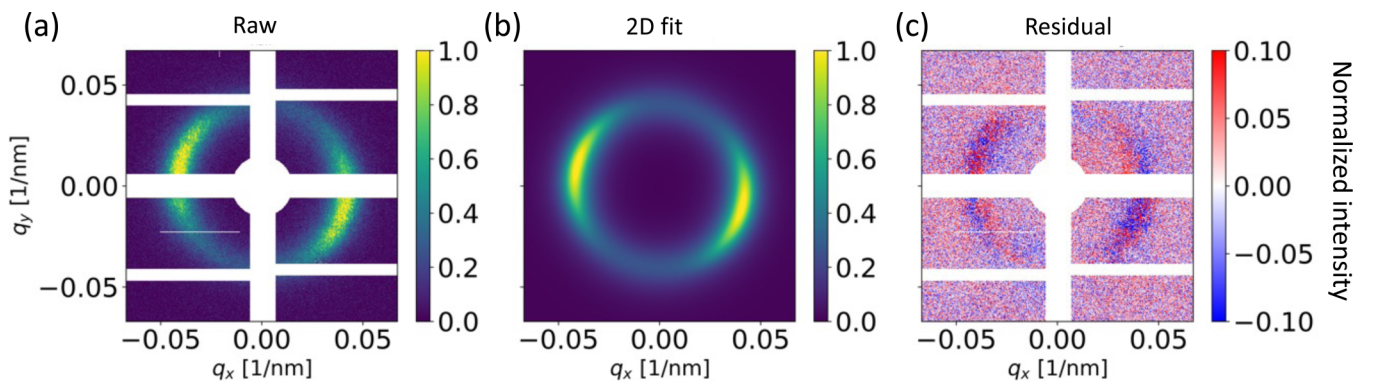


FIG. 9. (a) A raw image collected on the DSSC. (b) Two-dimensional fit of (a). The resulting residual (raw-fit) is shown in (c). Note that the intensity scale of the residual is one order of magnitude smaller than that of the raw scattering pattern.

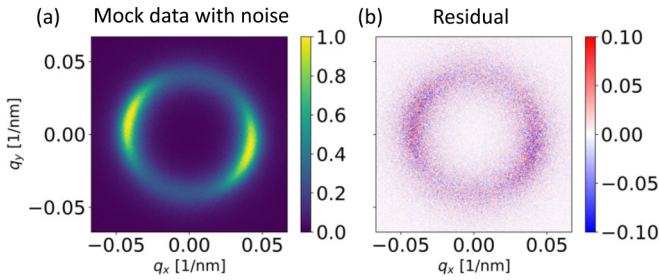


FIG. 10. (a) A mock scattering pattern. (b) The resulting residual of the 2D fit. Note that the intensity scale of the residual is one order of magnitude smaller than that of the raw scattering pattern.

By use of standard Fourier transform properties, we obtain the Fourier transform $F_1(q) = \mathcal{F}\{f_1(x)\}$ as

$$\begin{aligned}
 F_1(q) &= \frac{a}{2} \sum_n \left[\cos(\phi_n) e^{i\pi/2} + \sin(\phi_0) \right] e^{ina(q+q_n)/2} \text{sinc}\left(\frac{a(q+q_n)}{2\pi}\right) \\
 &\quad + \left[\cos(\phi_n) e^{-i\pi/2} + \sin(\phi_0) \right] e^{ina(q-q_n)/2} \text{sinc}\left(\frac{a(q-q_n)}{2\pi}\right). \quad (\text{D2})
 \end{aligned}$$

Therefore, the intensity is

$$\begin{aligned}
 |F_1(q)|^2 &= \frac{a^2}{4} \sum_n \text{sinc}^2\left(\frac{a(q+q_n)}{2\pi}\right) + \text{sinc}^2\left(\frac{a(q-q_n)}{2\pi}\right) \\
 &\quad + \frac{2a^2}{4} \sum_{n,m} \left[\cos(\phi_m - \phi_n - \frac{a}{2}(nq_n - mq_m)) \right. \\
 &\quad \left. \times \text{sinc}\left(\frac{a(q+q_n)}{2\pi}\right) \text{sinc}\left(\frac{a(q+q_m)}{2\pi}\right) \right]. \quad (\text{D3})
 \end{aligned}$$

The third term in Eq. (D3) represents a cross-term from the overlap of the sinc functions. If we assume that the periods between neighboring regions are similar, $q_n \approx q_m$, then only those regions where $n \approx m$ will contribute to the spectrum. If this were not the case, then overlap between the sinc functions would be small, and the cross-term would be negli-

gible. It follows that the cross-term is dominantly proportional to $\cos(\phi_m - \phi_n)$.

If the phase between neighboring regions is randomized, then the infinite sum over $\phi_m - \phi_n$ will span every phase between 0 and 2π . Therefore, the cross-term is zero. This situation is equivalent to consider that each region has a finite correlation length.

This toy model illustrates that the cross-term can be neglected for the ‘‘mixed’’ state, where the spatial periodicity is randomized.

APPENDIX E: PULSE-RESOLVED PHOTON COUNT IN THE SCATTERING DATA

The DSSC is a soft-x-ray detector with single-photon sensitivity and a frame rate that is able to match the pulse rate of the FEL [29]. The resulting scattering image, e.g., Fig. 11(a), is the average of all frames collected within a run. After multiplying by the gain of the detector, the intensity can be directly related to the average number of photons hitting each pixel per pulse. In our experiment, the gain was set to 0.5 photon/bin.

The 2D fit allows us to extrapolate the intensity in the areas with missing pixels as well as fully separate the isotropic from the anisotropic components. It is therefore possible to calculate the average number of photons per x-ray pulse contributing to the isotropic and anisotropic components by summing the intensity in the component image. In the example of Fig. 11, an average of 17.5 photons per pulse hit the detector where 9.5 photons belong to the isotropic contribution and 7.5 photons belong to the anisotropic contribution. The background contributes with an average of 0.5 photon/pulse. With 26 pulses per train at a train repetition rate of 10 Hz, we get 4550 photons per second in the full scattering with 2470 photons in the isotropic component, 1950 photons in the anisotropic component, and 130 photons in the background. Table III summarizes the photon count from all the pump-probe measurements.

In Sec. II B we explain how we categorize our data according to Eq. (4). Figure 12 shows the distribution of ratios for the collected data. We can clearly distinguish three groups that correspond to the three types of scattering that we observe. Due to the nonzero background, the isotropic scattering has a ratio close to 1 while anisotropic scattering has a ratio

TABLE II. Parameters of the phenomenological 2D fit function used to generate the mock data before adding shot noise [Fig. 10(a)]. In the initial guess, the anisotropic scattering radius q_1 is slightly shifted. This change is recovered by the 2D fit as shown in the last column.

Parameters	Mock data	Initial guess	Fitted parameters
B	6.66×10^{-6}	6.66×10^{-6}	$(6.62 \pm 0.03) \times 10^{-6}$
q_0	4.0183×10^{-2}	4.0183×10^{-2}	$(4.0188 \pm 0.0005) \times 10^{-2}$
Γ_0	1.448×10^{-2}	1.448×10^{-2}	$(1.451 \pm 0.001) \times 10^{-2}$
A_0	1.6052×10^{-2}	1.6052×10^{-2}	$(1.6050 \pm 0.0005) \times 10^{-2}$
q_1	4.2636×10^{-2}	4.2136×10^{-2}	$(4.2635 \pm 0.0002) \times 10^{-2}$
Γ_1	0.7011×10^{-2}	0.7011×10^{-2}	$(0.6991 \pm 0.0004) \times 10^{-2}$
$ A_1 $	2.8026×10^{-2}	2.8026×10^{-2}	$(2.8026 \pm 0.0007) \times 10^{-2}$
$ A_2 $	0.111×10^{-2}	0.111×10^{-2}	$(0.111 \pm 0.001) \times 10^{-2}$
φ	0.244	0.244	0.245 ± 0.002

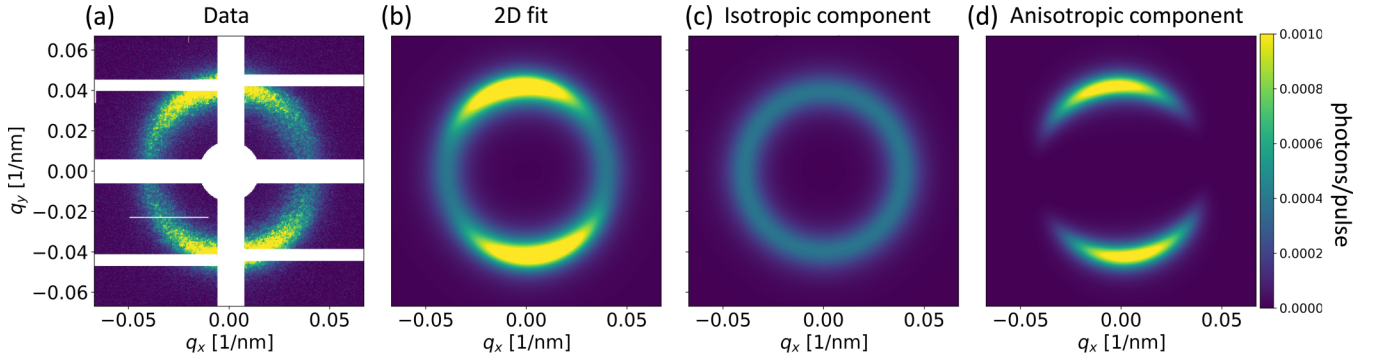


FIG. 11. (a) The raw data collected on the DSSC. The resulting two-dimensional fit (b) can be separated into ring component (c) and lobe component (d). The intensity colorbar is shared between all four panels and can be interpreted as photons/pixel/pulse.

close to -0.5 . We note that, because the anisotropic photons are more localized in space, fewer photons are required to observe anisotropic scattering, while more photons are needed in order to clearly observe isotropic scattering above the noise.

APPENDIX F: FITTING THE DEMAGNETIZATION CONSTANTS

The fitting procedure for extracting demagnetization values and time constants is explained in detail by Unikandanunni *et al.* We use the equation from [38]

$$\frac{\Delta M}{M_0} = \left(\frac{A_1 \tau_R - A_2 \tau_m}{\tau_R - \tau_m} e^{-(t-t_0)/\tau_m} - \frac{\tau_R(A_1 - A_2)}{\tau_R - \tau_m} e^{-(t-t_0)/\tau_R} - \frac{A_2}{\sqrt{(t-t_0)/\tau_R + 1}} \right) \otimes \Gamma(t), \quad (\text{F1})$$

where τ_m is the quench constant, τ_R is the recovery constant, and A_1 and A_2 are dimensionless constants related to the quench and recovery amplitudes. We fit t_0 , the time zero of the dynamics, in order to account for jitter in the pump arrival. The expression within parentheses is convoluted with a Gaussian $\Gamma(t)$ to account for the finite duration of the x-ray and IR pulses.

We disregard the second, algebraic recovery time Unikandanunni *et al.* used in their work since we did not collect data at long enough times to properly fit this value. Therefore, we use a simpler expression given by

$$f_{\text{quench}} = 1 + Ae^{-(t-t_0)/\tau_m} - Be^{-(t-t_0)/\tau_R} + B - A, \quad (\text{F2})$$

where the new coefficients, A and B , are related to the coefficients in Eq. (F1) by

$$A_1 = A - B \frac{\tau_m}{\tau_R}, \quad (\text{F3a})$$

$$A_2 = A - B. \quad (\text{F3b})$$

From this equation, we can analytically obtain the quench time by finding the minimum of f_{quench} , given by

$$t_{\min} = t_0 - \frac{\tau_m \tau_R}{\tau_R - \tau_m} \ln \left(\frac{B \tau_m}{A \tau_R} \right). \quad (\text{F4})$$

TABLE III. The average photon count is quantified per pulse and per second. For all the runs the XFEL delivered 26 pulses per train with a train repetition rate of 10 Hz. The average photon count in the full scattering is decomposed into the anisotropic and isotropic components as well as the uniform nonmagnetic background.

Run ID	Fluence	Total photons per pulse				Total photons per second			
		Full scattering	Anisotropic	Isotropic	Background	Full scattering	Anisotropic	Isotropic	Background
1	20 mJ cm ⁻² FO (day 3)	13.55	4.35	7.85	1.35	3523	1131	2041	351
2	15 mJ cm ⁻² FO (day 3)	14.30	4.55	8.4	1.35	3718	1183	2184	351
3	25 mJ cm ⁻² FO (day 4)	16.75	3.35	10.15	3.25	4355	871	2639	845
4	15 mJ cm ⁻² FO (day 4)	21.40	3.25	12.1	6.05	5564	845	3146	1573
5	15 mJ cm ⁻² FO (day 5)	18.38	12.21	5.29	0.88	4778	3175	1375	228
6	15 mJ cm ⁻² PO (day 5)	18.82	8.43	9.49	0.9	4891	2190	2467	234
7	15 mJ cm ⁻² PO (day 5)	22.21	0	21.18	1.03	5772	0	5507	267
8	10 mJ cm ⁻² FO (day 5)	20	0	18.35	1.65	5200	0	4771	429
9	10 mJ cm ⁻² FO (day 5)	18.95	13.34	4.84	0.77	4927	3468	1258	201

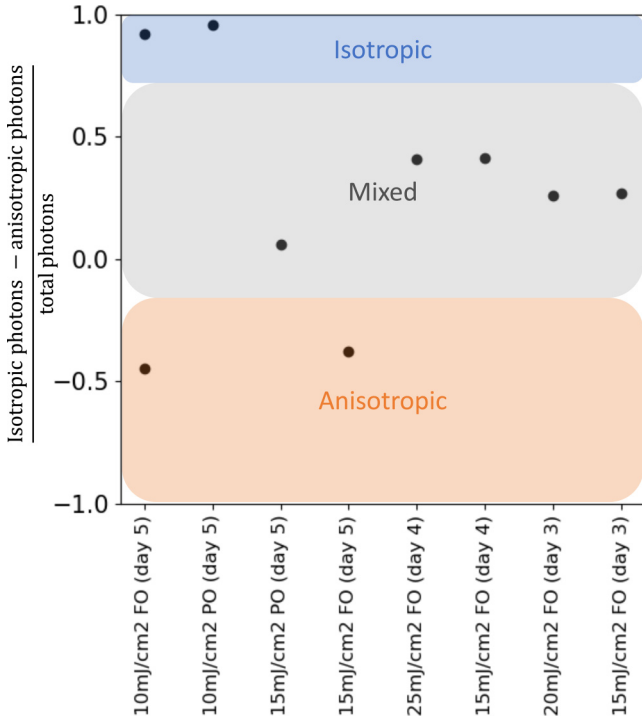


FIG. 12. Distribution of data according to categorization. The ratio is computed according to Eq. (4). Isotropic scattering has a ratio close to 1 while anisotropic scattering has a ratio close to -0.5 . For a ratio between -0.3 and 0.9 , we categorize the scattering pattern as mixed.

It follows that the error δt_{\min} can be computed by standard propagation of uncertainty for each fitted variable. The partial derivatives are

$$\frac{\partial t_{\min}}{\partial t_0} = \delta t_0, \quad (\text{F5a})$$

$$\frac{\partial t_{\min}}{\partial A} = \frac{\tau_m \tau_R}{\tau_R - \tau_m} \frac{\delta A}{A} \approx \frac{\tau_m}{A} \delta A, \quad (\text{F5b})$$

$$\frac{\partial t_{\min}}{\partial B} = \frac{\tau_m \tau_R}{\tau_R - \tau_m} \frac{\delta B}{B} \approx \frac{\tau_m}{B} \delta B, \quad (\text{F5c})$$

$$\begin{aligned} \frac{\partial t_{\min}}{\partial \tau_m} &= \frac{\tau_R}{\tau_R - \tau_m} \left[1 + \frac{\tau_R}{\tau_R - \tau_m} \ln \left(\frac{B \tau_m}{A \tau_R} \right) \right] \delta \tau_m \\ &\approx \left[1 + \ln \left(\frac{B \tau_m}{A \tau_R} \right) \right] \delta \tau_m, \end{aligned} \quad (\text{F5d})$$

$$\frac{\partial t_{\min}}{\partial \tau_R} = \frac{\tau_m}{\tau_R - \tau_m} \left[1 + \frac{\tau_m}{\tau_R - \tau_m} \ln \left(\frac{B \tau_m}{A \tau_R} \right) \right] \delta \tau_R \approx \frac{\tau_m}{\tau_R} \delta \tau_R. \quad (\text{F5e})$$

The approximations consider that $\tau_m \ll \tau_R$, but this leads to an infinite error in τ_m , so the approximation must be taken with care.

The quench is then f_{quench} evaluated at t_{\min} ,

$$A_q = A \left[1 - \left(\frac{B \tau_m}{A \tau_R} \right)^{\tau_R / (\tau_R - \tau_m)} \right] - B \left[1 - \left(\frac{B \tau_m}{A \tau_R} \right)^{\tau_m / (\tau_R - \tau_m)} \right], \quad (\text{F6})$$

and the error δA_q can be obtained from propagation of uncertainty of the following quantities:

$$\frac{\partial A_q}{\partial A} = \left[1 - \left(\frac{B \tau_m}{A \tau_R} \right)^{\tau_R / (\tau_R - \tau_m)} \right] \delta A \approx \delta A, \quad (\text{F7a})$$

$$\frac{\partial A_q}{\partial B} = \left[1 - \left(\frac{B \tau_m}{A \tau_R} \right)^{\tau_m / (\tau_R - \tau_m)} \right] \delta B, \quad (\text{F7b})$$

$$\begin{aligned} \frac{\partial A_q}{\partial \tau_R} &= \frac{1}{\tau_R (\tau_R - \tau_m)^2} \left\{ A \tau_R \left(\frac{B \tau_m}{A \tau_R} \right)^{\tau_R / (\tau_R - \tau_m)} \left[\tau_R - \tau_m + \tau_m \ln \left(\frac{B \tau_m}{A \tau_R} \right) \right] \right. \\ &\quad \left. - B \tau_m \left(\frac{B \tau_m}{A \tau_R} \right)^{\tau_m / (\tau_R - \tau_m)} \left[\tau_R - \tau_m + \tau_R \ln \left(\frac{B \tau_m}{A \tau_R} \right) \right] \right\} \delta \tau_R, \approx \frac{B \tau_m}{\tau_R^2} \delta \tau_R, \end{aligned} \quad (\text{F7c})$$

$$\begin{aligned} \frac{\partial A_q}{\partial \tau_m} &= \frac{1}{\tau_m (\tau_R - \tau_m)^2} \left\{ B \tau_m \left(\frac{B \tau_m}{A \tau_R} \right)^{\tau_m / (\tau_R - \tau_m)} \left[\tau_R - \tau_m + \tau_R \ln \left(\frac{B \tau_m}{A \tau_R} \right) \right] \right. \\ &\quad \left. - A \tau_R \left(\frac{B \tau_m}{A \tau_R} \right)^{\tau_R / (\tau_R - \tau_m)} \left[\tau_R - \tau_m + \tau_m \ln \left(\frac{B \tau_m}{A \tau_R} \right) \right] \right\} \delta \tau_m \approx \frac{B}{\tau_R} \delta \tau_m. \end{aligned} \quad (\text{F7d})$$

TABLE IV. Measurements are listed by pump fluence and scattering pattern. We distinguish between full overlap (FO) and partial overlap (PO) between probe and probe. Extracted domain size π/q (nm) and linewidth Γ (nm^{-1}) from the prepumped signal, maximum shift in radial peak position (%), maximum demagnetization (%), quench time (ps) and quench speed (ps^{-1}), and demagnetization recovery time (ps) for all measurements.

Run ID	Fluence	SAXS pattern	Isotropic component						
			Prepumped			Pumped			
			size (nm)	Γ (μm^{-1})	$\Delta q/q$ (%)	$\Delta M/M$ (%)	t_{\min} (ps)	quench speed (ps^{-1})	τ_R (ps)
1	20 mJ cm^{-2} FO (day 3)	mixed	78.30 \pm 0.11	1.482 \pm 0.012	1.0 \pm 0.4	43.5 \pm 0.9	0.714 \pm 0.033	60.9 \pm 3.1	3.16 \pm 0.27
2	15 mJ cm^{-2} FO (day 3)	mixed	77.27 \pm 0.14	1.679 \pm 0.017	1.5 \pm 0.6	29.3 \pm 1.0	0.660 \pm 0.039	44.4 \pm 3.0	2.80 \pm 0.23
3	25 mJ cm^{-2} FO (day 4)	mixed	71.96 \pm 0.34	2.572 \pm 0.055	3.5 \pm 2.3	38.2 \pm 1.4	0.970 \pm 0.049	39.4 \pm 2.5	2.05 \pm 0.17
4	15 mJ cm^{-2} FO (day 4)	mixed	71.86 \pm 0.28	2.534 \pm 0.045	2.7 \pm 2.7	21.2 \pm 1.0	0.738 \pm 0.012	28.7 \pm 1.4	1.73 \pm 0.18
6	15 mJ cm^{-2} PO (day 5)	mixed	77.56 \pm 0.04	1.086 \pm 0.004	1.88 \pm 0.07	21.9 \pm 0.7	0.610 \pm 0.02	35.8 \pm 1.8	1.29 \pm 0.07
7	10 mJ cm^{-2} PO (day 5)	isotropic	89.38 \pm 0.02	1.249 \pm 0.002	0.70 \pm 0.05	12.6 \pm 0.5	0.840 \pm 0.02	14.9 \pm 0.7	0.87 \pm 0.05
8	10 mJ cm^{-2} FO (day 5)	isotropic	76.66 \pm 0.01	0.953 \pm 0.002	0.84 \pm 0.06	38.5 \pm 0.8	0.964 \pm 0.02	39.9 \pm 1.2	1.57 \pm 0.03

TABLE V. Measurements are listed by pump fluence and scattering pattern. We distinguish between full overlap (FO) and partial overlap (PO) between probe and probe. Extracted domain size π/q (nm) and linewidth Γ (nm^{-1}) from the prepumped signal, maximum shift in radial peak position (%), maximum demagnetization (%), quench time (ps) and quench speed (ps^{-1}), and demagnetization recovery time (ps) for all measurements.

Run ID	Fluence	SAXS pattern	Anisotropic component						
			Prepumped			Pumped			
			size (nm)	Γ (μm^{-1})	$\Delta q/q$ (%)	$\Delta M/M$ (%)	t_{\min} (ps)	quench speed (ps^{-1})	τ_R (ps)
1	20 mJ cm^{-2} FO (day 3)	mixed	74.55 \pm 0.04	0.711 \pm 0.004	0	35.4 \pm 1.0	0.549 \pm 0.043	59.8 \pm 3.5	2.25 \pm 0.14
2	15 mJ cm^{-2} FO (day 3)	mixed	73.58 \pm 0.04	0.715 \pm 0.005	0	20.9 \pm 1.4	0.549 \pm 0.043	38.1 \pm 3.9	1.52 \pm 0.14
3	25 mJ cm^{-2} FO (day 4)	mixed	74.06 \pm 0.14	0.808 \pm 0.016	0.5 \pm 0.5	34.9 \pm 1.8	0.836 \pm 0.049	41.7 \pm 3.3	1.68 \pm 0.15
4	15 mJ cm^{-2} FO (day 4)	mixed	74.98 \pm 0.14	0.794 \pm 0.015	0	18.0 \pm 1.8	0.679 \pm 0.021	26.5 \pm 2.8	0.99 \pm 0.15
5	15 mJ cm^{-2} FO (day 5)	anisotropic	73.08 \pm 0.01	0.729 \pm 0.001	0	56.7 \pm 0.7	0.58 \pm 0.02	96.7 \pm 3.7	2.86 \pm 0.08
6	15 mJ cm^{-2} PO (day 5)	mixed	74.16 \pm 0.03	0.671 \pm 0.002	0.23 \pm 0.05	24.1 \pm 0.2	0.61 \pm 0.02	39.6 \pm 1.5	1.04 \pm 0.05
9	10 mJ cm^{-2} FO (day 5)	anisotropic	72.3 \pm 0.01	0.646 \pm 0.001	0	37.6 \pm 0.4	0.813 \pm 0.013	46.2 \pm 0.9	1.65 \pm 0.02

Tables IV and V show the extracted fitting parameters discussed in our work for all measurements performed during the experiment.

APPENDIX G: FLUENCE DEPENDENCE OF ULTRAFAST MAGNETIZATION DYNAMICS

The effect of pump fluence was investigated in two different ways in our samples. For the isotropic scattering, we were able to probe the sample at a 50 μm offset from the pump spot, which we denote “partial overlap” (PO), shown as light colored curves. We compare the results with the data shown in the main text, where the pump spot was aligned with the probe spot. The resulting normalized magnetization is shown in Fig. 13(a). We observe a three times weaker quench in the partial overlap case, consistent with an approximately two times weaker pump fluence given its Gaussian profile. For the anisotropic scattering shown in Fig. 13(b), we probed the sample at a higher fluence of 15 mJ cm^{-2} and we observed an expectedly larger quench of the demagnetization.

The peak positions for both scattering components are shown in Figs. 13(c) and 13(d). In all cases, only the isotropic component exhibits a shift. It is worth noting that this shift is observed even when the probe is offset. On the contrary, no shift is observed for the anisotropic component, even when pumped with a large fluence.

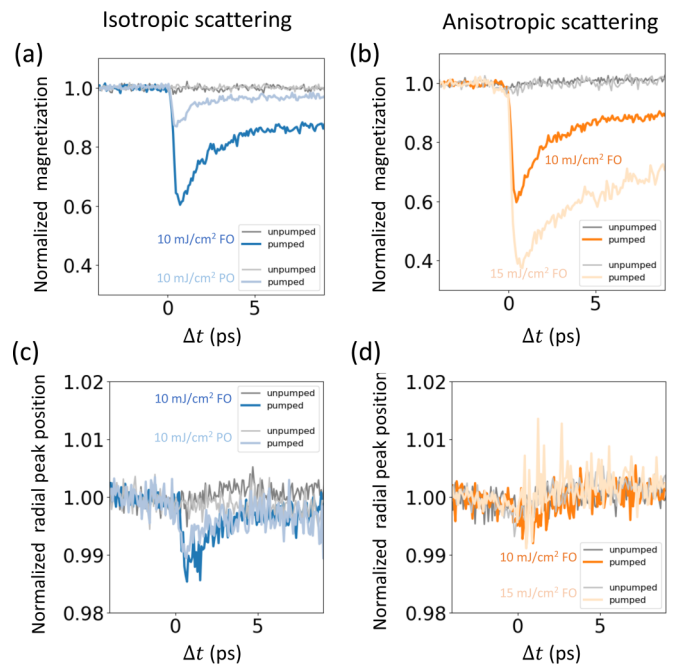


FIG. 13. Two-dimensional fitting of the full diffraction pattern is used to extract the time traces of both the magnetization and the peak position for the isotropic and anisotropic scattering patterns. In all panels, the gray curves represent the unpumped data. The normalized magnetization of isotropic and anisotropic scattering patterns is shown in (a) and (b), respectively. At a fluence of 10 mJ cm^{-2} , the magnetization is shown by the solid curves, also shown in the main text. We observe a similar amount of quenching in both cases. For the isotropic scattering, the effect of a spatial shift between the pump and probe spots exhibits a weaker amount of quenching due to a weaker optical pumping, shown by the light-colored curve labeled as partial overlap (PO). For the anisotropic component, a higher fluence of 15 mJ cm^{-2} results in a higher quench, shown by the light-colored curve. The corresponding temporal evolution of the scattering peak position is shown in (c) and (d) for the isotropic and anisotropic scattering patterns, respectively. Similar to the results shown in the main text, only the isotropic component exhibits a shift. The shaded areas in all cases correspond to the standard deviation of the fitted parameters.

- [1] M. Budden, T. Gebert, M. Buzzi, G. Jotzu, E. Wang, T. Matsuyama, G. Meier, Y. Laplace, D. Pontiroli, M. Riccò, F. Schlawin, D. Jaksch, and A. Cavalleri, *Nat. Phys.* **17**, 611 (2021).
- [2] M. Hase, P. Fons, K. Mitrofanov, A. V. Kolobov, and J. Tominaga, *Nat. Commun.* **6**, 8367 (2015).
- [3] E. J. Sie, C. M. Nyby, C. D. Pemmaraju, S. J. Park, X. Shen, J. Yang, M. C. Hoffmann, B. K. Ofori-Okai, R. Li, A. H. Reid, S. Weathersby, E. Mannebach, N. Finney, D. Rhodes, D. Chenet, A. Antony, L. Balicas, J. Hone, T. P. Devereaux, T. F. Heinz *et al.*, *Nature (London)* **565**, 61 (2019).
- [4] G. Coslovich, A. F. Kemper, S. Behl, B. Huber, H. A. Bechtel, T. Sasagawa, M. C. Martin, A. Lanzara, and R. A. Kaindl, *Sci. Adv.* **3**, e1600735 (2017).
- [5] F. Zhou, J. Williams, S. Sun, C. D. Malliakas, M. G. Kanatzidis, A. F. Kemper, and C.-Y. Ruan, *Nat. Commun.* **12**, 566 (2021).
- [6] Y. Wu, R. M. Young, M. Frasconi, S. T. Schneebeli, P. Spent, D. M. Gardner, K. E. Brown, F. Würthner, J. F. Stoddart, and M. R. Wasielewski, *J. Am. Chem. Soc.* **137**, 13236 (2015).
- [7] E. Iacocca, T.-M. Liu, A. H. Reid, Z. Fu, S. Ruta, P. W. Granitzka, E. Jal, S. Bonetti, A. X. Gray, C. E. Graves, R. Kukreja, Z. Chen, D. J. Higley, T. Chase, L. Le Guyader, K. Hirsch, H. Ohldag, W. F. Schlotter, G. L. Dakovski, G. Coslovich *et al.*, *Nat. Commun.* **10**, 1756 (2019).
- [8] F. Büttner, B. Pfau, M. Böttcher, M. Schneider, G. Mercurio, C. M. Günther, P. Hessian, C. Klose, A. Wittmann, K. Gerlinger, L.-M. Kern, C. Strüber, C. von K. Schmising, J. Fuchs, D. Engel, A. Churikova, S. Huang, D. Suzuki, I. Lemesch, M. Huang *et al.*, *Nat. Mater.* **20**, 30 (2021).
- [9] G. Berruto, I. Madan, Y. Murooka, G. M. Vanacore, E. Pomarico, J. Rajeswari, R. Lamb, P. Huang, A. J. Kruchkov,

- Y. Togawa, T. LaGrange, D. McGrouther, H. M. Rønnow, and F. Carbone, *Phys. Rev. Lett.* **120**, 117201 (2018).
- [10] A. Kirilyuk, A. V. Kimel, and T. Rasing, *Rev. Mod. Phys.* **82**, 2731 (2010).
- [11] C. E. Graves, A. H. Reid, T. Wang, B. Wu, S. de Jong, K. Vahaplar, I. Radu, D. P. Bernstein, M. Messerschmidt, L. Müller, R. Coffee, M. Bionta, S. W. Epp, R. Hartmann, N. Kimmel, G. Hauser, A. Hartmann, P. Holl, H. Gorke, J. H. Mantink *et al.*, *Nat. Mater.* **12**, 293 (2013).
- [12] P. Baláž, K. Carva, U. Ritzmann, P. Maldonado, and P. M. Oppeneer, *Phys. Rev. B* **101**, 174418 (2020).
- [13] E. Beaurepaire, J.-C. Merle, A. Daunois, and J.-Y. Bigot, *Phys. Rev. Lett.* **76**, 4250 (1996).
- [14] B. Koopmans, G. Malinowski, F. D. Longa, D. Steiauf, M. Fähnle, T. Roth, M. Cinchetti, and M. Aeschlimann, *Nat. Mater.* **9**, 259 (2010).
- [15] E. Turgut, C. La-o vorakiat, J. M. Shaw, P. Grychtol, H. T. Nembach, D. Rudolf, R. Adam, M. Aeschlimann, C. M. Schneider, T. J. Silva, M. M. Murnane, H. C. Kapteyn, and S. Mathias, *Phys. Rev. Lett.* **110**, 197201(2013).
- [16] B. Pfau, S. Schaffert, L. Müller, C. Gutt, A. Al-Shemmary, F. Büttner, R. Delaunay, S. Düsterer, S. Flewett, R. Frömter, J. Geilhufe, E. Guehrs, C. M. Günther, R. Hawaldar, M. Hille, N. Jaouen, A. Kobs, K. Li, J. Mohanty, H. Redlin *et al.*, *Nat. Commun.* **3**, 1100 (2012).
- [17] B. Vodungbo, J. Gautier, G. Lambert, A. B. Sardinha, M. Lozano, S. Sebban, M. Ducouso, W. Boutu, K. Li, B. Tudu, M. Tortarolo, R. Hawaldar, R. Delaunay, V. López-Flores, J. Arabski, C. Boeglin, H. Merdji, P. Zeitoun, and J. Lüning, *Nat. Commun.* **3**, 999 (2012).
- [18] P. Tengdin, W. You, C. Chen, X. Shi, D. Zusin, Y. Zhang, C. Gentry, A. Blonsky, M. Keller, P. M. Oppeneer, H. C. Kapteyn, Z. Tao, and M. M. Murnane, *Sci. Adv.* **4**, eaap9744 (2018).
- [19] M. Hennes, A. Merhe, X. Liu, D. Weder, C. von K. Schmising, M. Schneider, C. M. Günther, B. Mahieu, G. Malinowski, M. Hehn, D. Lacour, F. Capotondi, E. Pedersoli, I. P. Nikolov, V. Chardonnet, E. Jal, J. Lüning, and B. Vodungbo, *Phys. Rev. B* **102**, 174437 (2020).
- [20] D. Zusin, E. Iacocca, L. Le Guyader, A. H. Reid, W. F. Schlotter, T.-M. Liu, D. J. Higley, G. Coslovich, S. F. Wandel, P. M. Tengdin, S. K. K. Patel, A. Shabalyn, N. Hua, S. B. Hrkac, H. T. Nembach, J. M. Shaw, S. A. Montoya, A. Blonsky, C. Gentry, M. A. Hofer *et al.*, *Phys. Rev. B* **106**, 144422 (2022).
- [21] D. Turenne, A. Yaroslavtsev, X. Wang, V. Unikandanuni, I. Vaskivskiy, M. Schneider, E. Jal, R. Carley, G. Mercurio, R. Gort, N. Agarwal, B. V. Kuiken, L. Mercadier, J. Schlappa, L. Le Guyader, N. Gerasimova, M. Teichmann, D. Lomidze, A. Castoldi, D. Potorochin *et al.*, *Sci. Adv.* **8**, eabn0523 (2022).
- [22] I. Žutić, J. Fabian, and S. Das Sarma, *Rev. Mod. Phys.* **76**, 323 (2004).
- [23] S. Jeppson and R. Kukreja, *APL Mater.* **9**, 100702 (2021).
- [24] T. W. Hiscock and S. G. Megason, *Development* **142**, 409 (2015).
- [25] C. Léveillé, E. Burgos-Parra, Y. Sassi, F. Ajejas, V. Chardonnet, E. Pedersoli, F. Capotondi, G. De Ninno, F. Maccherozzi, S. Dhesi, D. M. Burn, G. van der Laan, O. S. Latcham, A. V. Shytov, V. V. Kruglyak, E. Jal, V. Cros, J.-Y. Chauléau, N. Reyren, M. Viret *et al.*, *Nat. Commun.* **13**, 1412 (2022).
- [26] J. M. Shaw, H. T. Nembach, and T. J. Silva, *Phys. Rev. B* **87**, 054416 (2013).
- [27] T. Tschentscher, C. Bressler, J. Grünert, A. Madsen, A. Mancuso, M. Meyer, A. Scherz, H. Sinn, and U. Zastra, *Appl. Sci.* **7**, 592 (2017).
- [28] T. Maltezopoulos, F. Dietrich, W. Freund, U. F. Jastrow, A. Koch, J. Laksman, J. Liu, M. Planas, A. A. Sorokin, K. Tiedtke, and J. Grünert, *J. Synch. Radiat.* **26**, 1045 (2019).
- [29] M. Porro, L. Andricek, S. Aschauer, A. Castoldi, M. Donato, J. Engelke, F. Erdinger, C. Fiorini, P. Fischer, H. Graafsma, A. Grande, C. Guazzoni, K. Hansen, S. Hauf, P. Kalavakuru, H. Klaer, M. Tangl, A. Kugel, M. Kuster, P. Lechner *et al.*, *IEEE Trans. Nucl. Sci.* **68**, 1334 (2021).
- [30] N. Zhou Hagström, M. Schneider, N. Kerber, A. Yaroslavtsev, E. Burgos Parra, M. Beg, M. Lang, C. M. Günther, B. Seng, F. Kammerbauer, H. Popescu, M. Pancaldi, K. Neeraj, D. Polley, R. Jangid, S. B. Hrkac, S. K. K. Patel, S. Ovcharenko, D. Turenne, D. Ksenzov *et al.*, *J. Synch. Radiat.* **29**, 1454 (2022).
- [31] M. Pergament, G. Palmer, M. Kellert, K. Kruse, J. Wang, L. Wissmann, U. Wegner, M. Emons, D. Kane, G. Priebe, S. Venkatesan, T. Jezynski, F. Pallas, and M. J. Lederer, *Opt. Express* **24**, 29349 (2016).
- [32] O. Hellwig, G. P. Denbeaux, J. B. Kortright, and E. E. Fullerton, *Phys. B: Condens. Matter* **336**, 136 (2003).
- [33] J. B. Kortright, S.-K. Kim, G. P. Denbeaux, G. Zeltzer, K. Takano, and E. E. Fullerton, *Phys. Rev. B* **64**, 092401 (2001).
- [34] J. Stöhr and H. C. Siegmann, *Magnetism: From Fundamentals to Nanoscale Dynamics* (Springer, Berlin, Heidelberg, New York, 2006).
- [35] J. B. Kortright, *J. Electron Spectrosc. Relat. Phenom.* **189**, 178 (2013).
- [36] M. F. Tesch, M. C. Gilbert, H.-C. Mertins, D. E. Bürgler, U. Berges, and C. M. Schneider, *Appl. Opt.* **52**, 4294 (2013).
- [37] N. Kerber, D. Ksenzov, F. Freimuth, F. Capotondi, E. Pedersoli, I. Lopez-Quintas, B. Seng, J. Cramer, K. Litzius, D. Lacour, H. Zabel, Y. Mokrousov, M. Kläui, and C. Gutt, *Nat. Commun.* **11**, 6304 (2020).
- [38] V. Unikandanunni, R. Medapalli, E. E. Fullerton, K. Carva, P. M. Oppeneer, and S. Bonetti, *Appl. Phys. Lett.* **118**, 232404 (2021).
- [39] E. Jal, M. Makita, B. Rösner, C. David, F. Nolting, J. Raabe, T. Savchenko, A. Kleibert, F. Capotondi, E. Pedersoli, L. Raimondi, M. Manfredda, I. Nikolov, X. Liu, A. el dine Merhe, N. Jaouen, J. Gorchon, G. Malinowski, M. Hehn, B. Vodungbo *et al.*, *Phys. Rev. B* **99**, 144305 (2019).
- [40] V. Cardin, T. Balciunas, K. Légaré, A. Baltuska, H. Ibrahim, E. Jal, B. Vodungbo, N. Jaouen, C. Varin, J. Lüning, and F. Légaré, *Phys. Rev. B* **101**, 054430 (2020).
- [41] X. Liu, A. Merhe, E. Jal, R. Delaunay, R. Jarrier, V. Chardonnet, M. Hennes, S. G. Chiuzbaian, K. Légaré, M. Hennecke, I. Radu, C. V. K. Schmising, S. Grunewald, M. Kuhlmann, J. Lüning, and B. Vodungbo, *Opt. Express* **29**, 32388 (2021).
- [42] M. Rühle and M. Wilkens, *Physical Metallurgy*, 4th ed., edited by R. W. Cahn and P. Haasen (North-Holland, Oxford, 1996), pp. 1033–1113.
- [43] V. Raposo, F. García-Sánchez, U. Atxitia, and E. Martínez, *Phys. Rev. B* **105**, 104432 (2022).
- [44] J. H. Mentink, J. Hellsvik, D. V. Afanasiev, B. A. Ivanov, A. Kirilyuk, A. V. Kimel, O. Eriksson, M. I. Katsnelson, and T. Rasing, *Phys. Rev. Lett.* **108**, 057202 (2012).
- [45] M. Battiato, K. Carva, and P. M. Oppeneer, *Phys. Rev. Lett.* **105**, 027203 (2010).

- [46] G. A. El and M. A. Hofer, *Physica D* **333**, 11 (2016).
- [47] M. Yan, A. Kákay, C. Andreas, and R. Hertel, *Phys. Rev. B* **88**, 220412(R) (2013).
- [48] E. Iacocca, T. J. Silva, and M. A. Hofer, *Phys. Rev. Lett.* **118**, 017203 (2017).
- [49] E. Iacocca and M. A. Hofer, *Phys. Rev. B* **95**, 134409 (2017).
- [50] M. Hu, E. Iacocca, and M. A. Hofer, *Phys. Rev. B* **105**, 104419 (2022).
- [51] D. Abdul-Wahab, E. Iacocca, R. F. L. Evans, A. Bedoya-Pinto, S. Parkin, K. S. Novoselov, and E. J. G. Santos, *Appl. Phys. Rev.* **8**, 041411 (2021).
- [52] P. A. P. Janantha, P. Sprenger, M. A. Hofer, and M. Wu, *Phys. Rev. Lett.* **119**, 024101 (2017).
- [53] P. Bruno and V. K. Dugaev, *Phys. Rev. B* **72**, 241302(R) (2005).
- [54] <https://in.xfel.eu/metadata/doi/10.22003/XFEL.EU-DATA-002719-00>; doi: 10.22003/XFEL.EU-DATA-002719-00.